scientific reports

OPEN

Coalescence and mixing dynamics of droplets in acoustic levitation by selective colour imaging and measurement

Kota Honda[1], Kota Fujiwara[1], Koji Hasegawa [2], Akiko Kaneko [3]✉ & Yutaka Abe[4]

Acoustic levitation is well-suited to 'lab-on-a-drop' contactless chemical analysis of droplets. Rapid mixing is of fundamental importance in lab-on-a-drop platforms and many other applications involving droplet manipulation. Small droplets, however, have low Reynolds numbers; thus, mixing via turbulence is not possible. Inducing surface oscillation is effective in this regard, however, the relationship between internal flow and mixing dynamics of droplets remains unclear. In this study, we conducted a set of simultaneous optical measurements to assess both the flow field and the distribution of fluid components within acoustically levitated droplets. To achieve this, we developed a technique to selectively separate fluorescent particles within each fluid, permitting the measurement of the concentration field based on the data from the discrete particle distribution. This approach revealed a relationship between the mixing process and the internal flow caused by surface oscillation. Thus, the internal flow induced by surface oscillation could enhance droplet mixing. Our findings will be conducive to the application and further development of lab-on-a-drop devices.

'Lab-on-a-drop' platforms present the possibility of performing contact-free chemical and physical analyses on nanolitre- to microlitre-sized droplets suspended in air[1–12]. The suspension of droplets is typically achieved through acoustic levitation using ultrasonic waves[13–16]—the 'acoustic tweezers' approach to lab-on-a-drop platform design[1]. In recent years, holographic technology combining multiple low-power transducers has made it possible to control the position of objects in mid-air using ultrasound[17–21]. Macromolecular X-ray diffraction analysis[10], Raman spectroscopy[6,7], and DNA transfection[12] have been conducted on acoustically levitated droplets. Contactless fluid manipulation is essential; therefore, several techniques have been proposed for droplet injection, levitation, transportation, coalescence, evaporation, and ejection[22–25]. Mixing, which is essential for diluting the sample and promoting chemical and biological reactions, is particularly challenging[26,27]: In a microlitre-sized droplet, the Reynolds number of the flow is very small (at most 2) while the Péclet number can be relatively high (10^2–10^5). This indicates that, despite the droplet's small size, neither molecular diffusion nor mixing via turbulence alone can completely homogenise the components of a droplet over a realistic length of time[28].

To prevent atmospheric contamination and changes in the concentration of the solution, the mixing time should be minimised[12,29,30]. This has been achieved by inducing sectorial oscillations at the droplet surface[22]. However, to further reduce the mixing time and expand the scope of industrial applications, the contactless-mixing mechanism in droplets needs to be explored in detail. Some experimental and theoretical investigations of this mechanism have been previously conducted[31–35]. Although a theoretical model of the interaction between molecular diffusion and mixing by advection has been proposed[31], molecular diffusion does not seem to play a major role in reducing the mixing time. The effects of surface oscillation and internal flow have also been theoretically predicted[31]. The importance of the temporal asymmetry of modal oscillation at the surface has been clarified[33]; however, the interaction between flow and mixing has not yet been elucidated beyond the fact that the radial flow due to oscillations imposed at the surface plays a vital role in mixing[33–35]. In addition, the coalescence and mixing of droplets is generally assumed in lab-on-a-drop applications to mix multiple types of liquids. Various studies have been conducted on droplet coalescence, including internal flow, external flow, and

[1]Graduate School of Science and Technology, University of Tsukuba, Tsukuba 305-8573, Japan. [2]Department of Mechanical Engineering, Kogakuin University, Tokyo 163-8677, Japan. [3]Institute of Systems and Information Engineering, University of Tsukuba, Tsukuba 305-8573, Japan. [4]Professor Emeritus, University of Tsukuba, Tsukuba 305-8573, Japan. ✉email: kaneko@kz.tsukuba.ac.jp

the bridge formed between droplets[36–46]. However, to our knowledge, there are no studies investigating the flow and mixing that occurs during droplet coalescence.

Therefore, a better empirical understanding of the relationship between internal flow and droplet mixing is needed. In general, the homogenisation of components by mixing can be achieved in three ways: the stretching of fluid components by the flow field, diffusion by molecular motion, and atomisation of droplets by interfacial tension[47]. If the flow and local distribution of fluid components inside a droplet can be measured, the mechanism underlying mixing enhancement can be elucidated. However, there is a practical limitation on the simultaneous measurement of component distribution and flow field inside a droplet.

Typically, flow field and mixing measurements are carried out in separate experiments under identical conditions[48]. However, to evaluate the influence of the flow field on mixing dynamics, consistent visualization techniques are essential for measuring both velocity and concentration fields. Particle image velocimetry (PIV) is usually employed to visualize the internal flow field. There are numerous visualization techniques designed to study fluid mixing, which can be classified according to their spatial dimension of measurement. For instance, the 3D tomography methods employing gamma rays and X-rays are widely recognised, but their requirement for relatively large equipment and their insufficient spatial resolution make them unsuitable for droplets of a few millimetres in diameter, as in this study[49]. An alternative method involves the use of fluorescent dyes to gauge the degree of mixing through image processing[50]. Although this method is more cost-effective and offers superior spatial resolution, a potential issue arises when both fluorescent dyes and tracer particles are used in the same system. This could lead to interference between the luminance information of the two components. To circumvent this interference, an innovative approach could involve developing a technique to selectively separate particles within each fluid and measure the concentration field using information from the discrete particle distribution. If the particles used for PIV could also serve as markers for concentration field measurement, such a solution could be feasible. With this concept, the authors aim to develop a method that can simultaneously measure both velocity and concentration fields within a small droplet, while preserving comparable spatial and temporal resolution.

To elucidate the relationship between internal flow and mixing when oscillation is applied on the surface, herein, the surface shape, particle distributions, and flow fields in acoustically levitated droplets before and after coalescence were simultaneously analysed in detail using a novel visualisation method. The distribution of fluid elements within two droplets was visualised by selectively illuminating fluorescent particles of two different colours. This was achieved by employing red and green fluorescent particles, which were captured using a pair of synchronized high-speed cameras equipped with optical filters. Droplet coalescence and the mixing process were observed in three regimes: immediately before and after coalescence, during oscillation, and when the oscillation settled. For each timescale, the number-fraction distribution of the two types of particles was calculated to evaluate the degree of mixing. For the visualisation of flow fields, PIV was conducted for each regime to obtain velocity information about the droplets. Finally, to demonstrate the mixing performance of acoustic levitation, mixing indices were calculated on the basis of number-fraction distribution of particles. These results and the proposed method should be helpful in understanding droplet mixing dynamics and contribute to the optimisation of the acoustic-tweezers lab-on-a-drop platform.

Results and discussions
General observation of mixing in droplets
Two droplets were levitated in mid-air by utilising acoustic radiation pressure, each positioned at one of two ultrasound focal points. The droplets were then purposefully merged by reducing the distance between these two focal points, resulting in a single droplet (Fig. 1). From $t = -1.5$ to 12.4 ms, this process could be seen in the observation window. However, owing to the displacement caused by coalescence, the droplet began to move
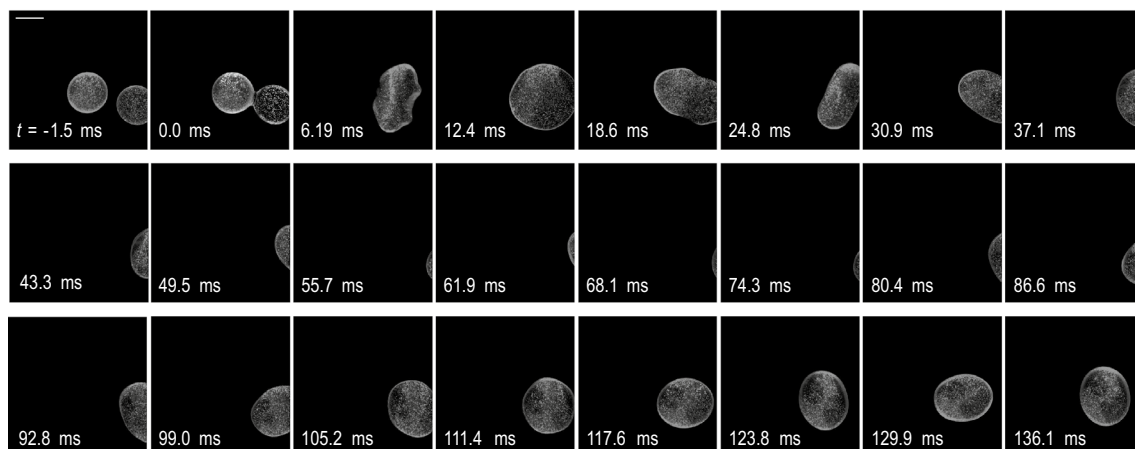
Figure 1. Coalescence of two ethanol droplets. Each image is a combination of images taken by two high-speed video cameras. Scale bar represents 1 mm. At time $t = 0$, two droplets start to coalesce.

out of the frame at $t = 12.4–49.5$ ms. It was mostly unobservable from 55.7 to 74.3 ms but returned to view at 80.4–117.6 ms.

There were bright and dark areas within the droplet owing to the fluorescence of the particles. At $t = −1.5$ ms, immediately before they merged, the two droplets were clearly distinguishable by their brightness difference. From 6.19 to 30.9 ms, it was still possible to distinguish the brightness distributions in the merged droplet. However, from 105.2 to 136.1 ms, the brightness distribution exhibited a complex pattern. These changes indicate that the component originating from each of the two droplets spread over the entire droplet with time. Therefore, the local concentration of each component could be quantitatively identified from the particle distribution.

The droplet achieved a distorted shape at $t = 6.19$ ms. From 12.4 to 30.9 ms, it periodically changed its elongation direction. From 99.0 to 136.0 ms, the degree of elongation gradually decreased.

Droplet coalescence

The behaviour of droplets immediately before and after coalescence is shown in Fig. 2. In Fig. 2-i (and in similar figures shown later in the paper), the image that captured light with a short wavelength is coloured green while the image that captured light with a long wavelength is shown in red. The surface shapes of the ethanol and glycerol-water solution droplets were distorted after coalescence. On the other hand, the surface shape of the
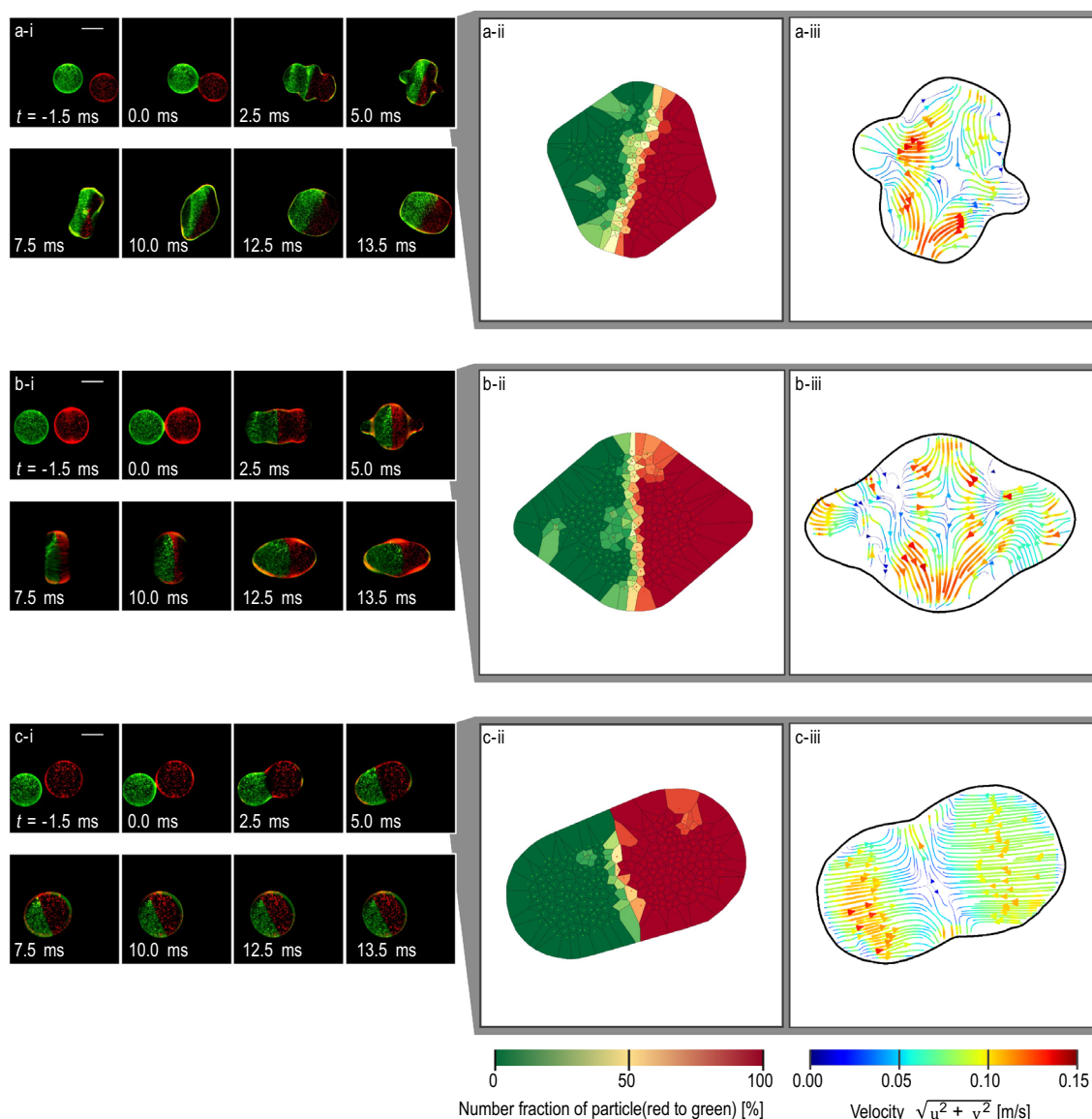
Figure 2. Visualisation of mixing process, number fraction of particles, and flow field in droplets immediately before and after coalescence. Coalescence of two (**a**) ethanol droplets, (**b**) 33 wt% glycerol–water solution droplets, and (**c**) pure glycerol droplets. (**i**) Photographs. (**ii**) Number fraction of particles (red and green dots) inside a droplet. (**iii**) Flow field of a droplet. For (**a-c**), (**ii**) and (**iii**) were calculated from the snapshot at $t = 5.0$ ms. Scale bar indicates 1 mm. (**a-i**), (**b-i**), and (**c-i**) correspond to Supplementary video S1, S2, and S3, respectively. At $t = 0$, two droplets start coalescing.

3

pure glycerol droplet remained circular. From Fig. 2a-i, at $t = -1.5$ ms, it can be seen that the two component droplets were clearly distinguishable by the red and green particles. During coalescence, at $t = 2.5$ ms, the green and red particles were distributed on the left and right sides, respectively, of the droplet. Thus, the components of the droplet could be visualized using the two monochrome cameras and optical filters.

The distribution of the particle-number fraction at $t = 5.0$ ms is shown in Fig. 2-ii for each case in a-c. As shown in Fig. 2-i, until $t = 13.5$ ms, the green and red particles were distributed on the left and right sides, respectively, of each droplet. This was reflected in the number-density distributions (except in the middle of each droplet, i.e., the contact area of the two original droplets, wherein cells with number fractions close to 50% were predominant). Therefore, both the images of the particles detected and number-fraction distributions reflected the expected distribution of particles.

Figure 2-iii shows the velocity field inside each droplet. In all three cases, coalescence produced opposing horizontal flow. Moreover, the flow sometimes changed direction from left–right to up–down. Considering the similarity of this to the case of a droplet with surface oscillation induced[22,35], the flow was probably caused by the deformation of the surface.

The maximum velocity in Fig. 2a-iii and b-iii was 0.15 m/s while that in Fig. 2c-iii was 0.10 m/s. Therefore, the maximum velocity was different for droplets with different compositions.

Surface oscillation of the droplet

The behaviour of the droplets from $t = 14.7$ ms to 30.0 ms is shown in Fig. 3. The direction of elongation changed periodically (Fig. 3a-i and b-i). By contrast, there was no deformation of the pure glycerol droplet (Fig. 3c-i). The time dependence of the amplitude, A, of surface oscillation of the droplets is[51]

$$A \propto e^{-\frac{t}{\tau_n}},$$
$$\text{where } \frac{1}{\tau_n} = \frac{\nu}{r^2}(n-1)(2n+1), \tag{1}$$

where t represents the time, ν, the kinematic viscosity, r, the volume-equivalent radius, and n, the mode of oscillation. Thus, increasing the viscosity of the droplets also increases the damping effect of surface oscillation. It can be seen from Fig. 3-i that for the 2nd mode oscillation, the width of each droplet was 2–3 mm. Owing to the acoustic radiation pressure, they were oblate horizontally; therefore, the height had a weaker effect on their volume than width. Thus, the droplets in this study were not expected to have significant differences in volume or volume-equivalent diameter R. In contrast, under the experimental conditions, the kinematic viscosities were 1.387×10^{-6}, 2.715×10^{-6}, and 720.0×10^{-6} m/s for ethanol, 33 wt% glycerol–water solution, and pure glycerol, respectively. Therefore, the damping effect of surface oscillation was twice as strong for the 33 wt% glycerol–water solution and 720 times stronger for pure glycerol than that for ethanol. These results confirmed that the difference in surface oscillation during coalescence was due to the difference in the droplets' kinematic viscosities.

The distribution of the particle-number fraction at $t = 21.3$ ms (Fig. 3-ii) was different from that at $t = 5.0$ ms (Fig. 2-ii). For all three cases in Fig. 3-i, although the green and red particles were concentrated on the left and right sides, respectively, of the droplet, the area with number fraction close to 50% was much larger than that observed in Fig. 2. This indicates that the mixing progressed with time.

Figure 3-iii shows the velocity field inside the droplets. A radial flow still existed in ethanol and the 33 wt% glycerol–water solution (Fig. 3a-iii and b-iii, respectively), and the maximum velocity of the flow was 0.15 m/s for both droplets. However, in the pure glycerol droplet shown in Fig. 3c-iii, there was only circumferential flow caused by the rotation of the droplet. Therefore, the velocity of the flow decreased near the centre. In a previous study[25,35], a relationship was found between the surface oscillation and internal flow of a droplet. Thus, in this study, the internal flow of the droplet was attributable to the oscillation at the surface.

Stable levitation after oscillation

The behaviour of the droplet after surface oscillation reached steady state is shown in Fig. 4. In ethanol (Fig. 4a-i), the distribution of the green and red particles was more complex at $t = 125$ ms than at $t = 21.3$ ms (Fig. 3a-ii), and the complexity increased as time passed. Finally, at $t = 300$ ms, the two types of particles were randomly distributed. In contrast, in the 33 wt% glycerol–water solution and pure glycerol (Fig. 4b-ii and c-ii, respectively), the two types of particles were still separated even at $t = 300$ ms. Specifically, in the pure glycerol droplet (Fig. 4c-ii), they remained segregated into opposite hemispheres.

The surface deformation still existed in the ethanol droplet at $t = 175$ ms shown in Fig. 4a-i. In contrast, the droplets of the 33 wt% glycerol–water solution and pure glycerol (Fig. 4b-i and c-i, respectively) were nearly spherical.

Different rates of mixing were also reflected in the number-fraction distribution of the particles shown in Fig. 4-ii. For ethanol (Fig. 4a-ii), cells with number fractions close to 50% were observed throughout the entire droplet. However, for the 33 wt% glycerol–water solution (Fig. 4b-ii), cells with number fractions close to 50% had a bow-shaped distribution in the lower right corner of the droplet; the change in the distribution was due to the internal flow. Finally, for pure glycerol (Fig. 4c-ii), the distribution was the same as that observed at $t = 21.3$ ms shown in Fig. 3c-ii.

Finally, Fig. 4-iii shows the velocity field inside each droplet. For all three cases, there was only circumferential flow.
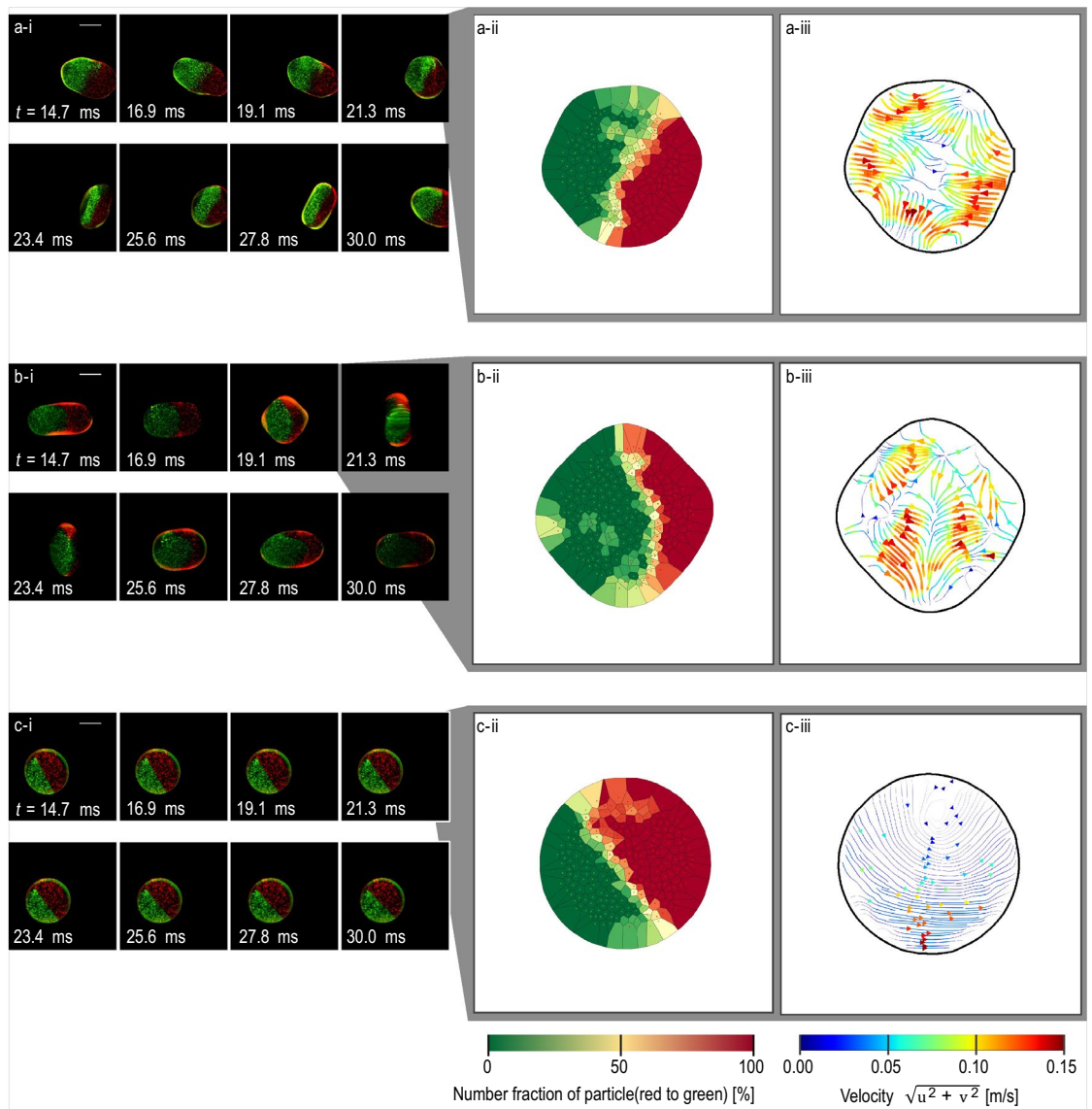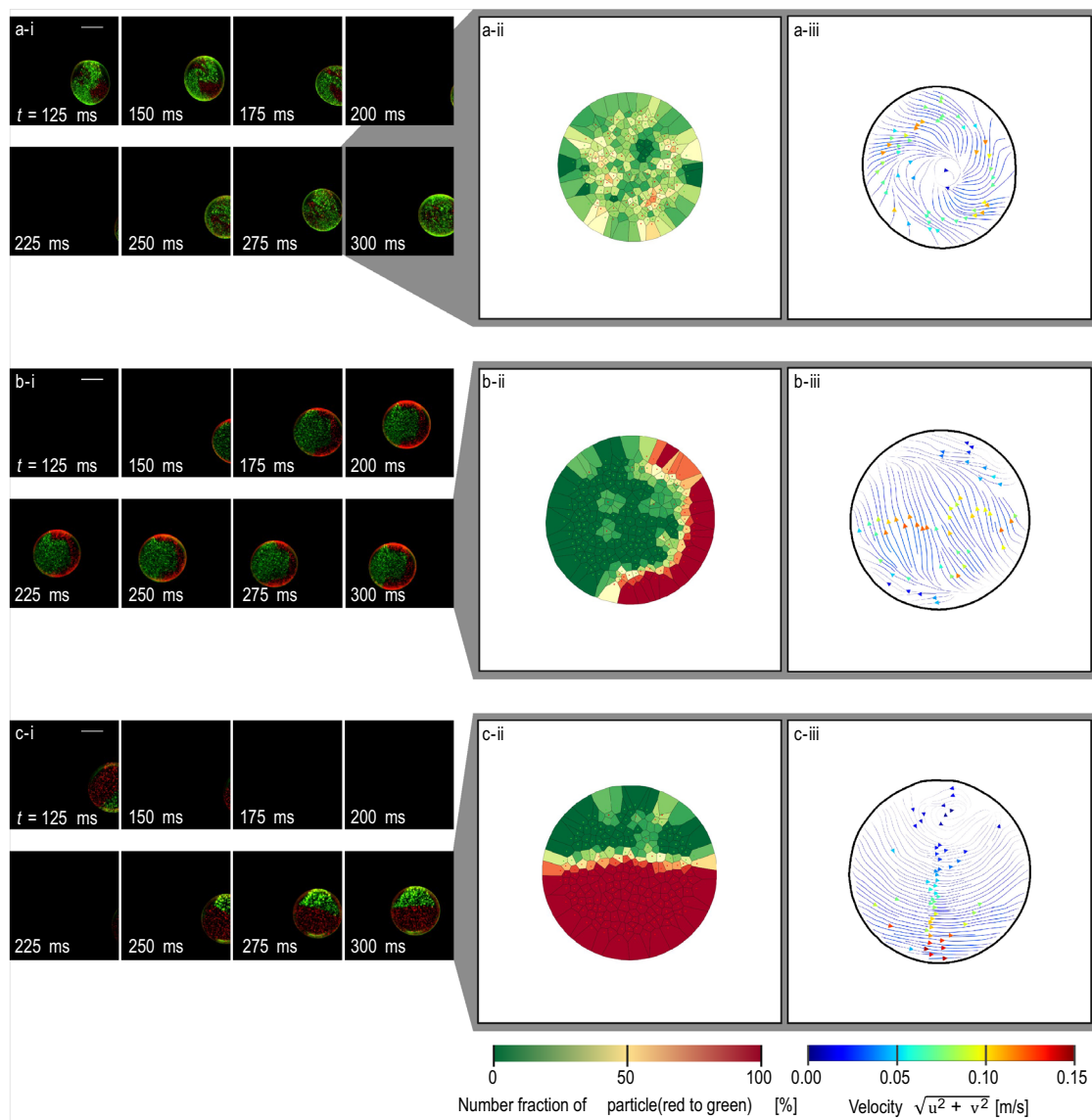
Figure 3. Visualisation of mixing process, number fraction of particles, and flow field in droplets during oscillation. Droplets formed from (**a**) two ethanol droplets, (**b**) two 33 wt% glycerol–water solution droplets, and (**c**) two pure glycerol droplets. (**i**) Photographs. (**ii**) Number fraction of particles (red and green dots) inside a droplet. (**iii**) Flow field of a droplet. For (**a**) and (**c**), (**ii**) and (**iii**) were calculated from the snapshot at $t = 19.1$ and 21.3 ms. For (**b**), (**ii**) and (**iii**) were calculated from the snapshot at $t = 19.1$ ms. Scale bar indicates 1 mm. At $t = 0$, two droplets start coalescing. (**a-i**), (**b-i**), and (**c-i**) correspond to Supplementary video S4, S5, and S6, respectively.

Quantification of mixing performance

To quantify the degree of mixing, the Lacey mixing index, Mc[52,53], was calculated for each droplet from the number-fraction distribution (Fig. 5); $Mc = 0.0$ corresponds to a completely separated state while $Mc = 1.0$ corresponds to a completely mixed one. For all three droplets, $Mc < 0.1$ immediately after coalescence. The Mc of ethanol was very close to 1 at 300 ms, which indicates that the two components originating from separate ethanol droplets had become randomly distributed. In contrast, the Mc's of the glycerol–water solution and pure glycerol droplets were 0.5 and 0.2, respectively, at 300 ms. This trend was qualitatively similar to that observed for the degree of mixing after coalescence, at 300 ms (Fig. 4). In addition, all three Mc's increased with time. This indicates that the Mc's reflected the actual mixing states of the component droplets, i.e., the degree of mixing was successfully quantified.

For ethanol, Mc increased from 0.1 to 0.4 until $t = 30$ ms, then gradually increased from 0.4 to 1.0 until $t = 300$ ms. For $t < 30$ ms, the surface exhibited significant oscillation (Figs. 2a-i and 3a-i). Although surface oscillation subsided with time, it still existed at $t = 175$ ms, as shown in Fig. 4a-i.

Figure 4. Visualisation of mixing process, number fraction of particles, and flow field in droplets after oscillation. Droplet formed from (**a**) two ethanol droplets, (**b**) two 33 wt% glycerol–water solution droplets, and (**c**) two pure glycerol droplets. (**i**) Photographs. (**ii**) Number fraction of particles (red and green dots) inside a droplet. (**iii**) Flow field of a droplet. For (**a**), (**ii**) and (**iii**) were calculated from the snapshot at $t = 275$ and 300 ms. For (**b**) and (**c**), (**ii**) and (**iii**) were calculated from the snapshot at $t = 300$ ms. Scale bar indicates 1 mm. At $t = 0$, two droplets start coalescing. (**a-i**), (**b-i**), and (**c-i**) correspond to Supplementary video S7, S8, and S9, respectively.

For the 33 wt% glycerol–water solution droplet, Mc increased from 0.1 to 0.5 until $t = 50$ ms, after which it stayed relatively constant. As in the case of ethanol droplets, the surface also exhibited significant oscillation for $t < 30$ ms (Figs. 2a-i and 3a-i). However, surface oscillation of the interface was negligible at $t = 175$ ms (Fig. 4b-i).

Finally, for the pure glycerol droplet, Mc increased from 0.1 to 0.2 until $t = 10$ ms, maintaining that value thereafter. From $t = 0.0$ to 7.5 ms, the contact area of the original droplet component increased (Fig. 2c-i). Thereafter, no oscillation was observed at the surface (Figs. 2c-i, 3c-i, 4c-i).

The contrasting observations made between the Mc and droplet behaviour suggests three possible factors that led to the increase the Mc. The first factor was the increase in the contact area of the original droplet components due to coalescence of the droplets. In this study, no oscillation was observed at the surface of pure glycerol droplet. However, a comparison of Fig. 5 with Fig. 2c-i shows that for the pure glycerol droplet, Mc increased from 0.1 to 0.2 as the two droplets coalesced into a single droplet from $t = 0.0$ to 7.5 ms. The second factor was the intensity of surface oscillation: for $t < 30.0$ ms (Figs. 2 and 3), oscillation at the surface were present in the ethanol and 33 wt% glycerol–water solution droplets, with $Mc = 0.4$ at around $t = 30.0$ ms. In contrast, surface oscillation was absent in the pure glycerol droplet with $Mc = 0.2$. The final factor was the duration of surface oscillation. Specifically, at $t = 300.0$ ms, $Mc = 1.0$ for the ethanol droplet, for which oscillations at the surface were still observed at
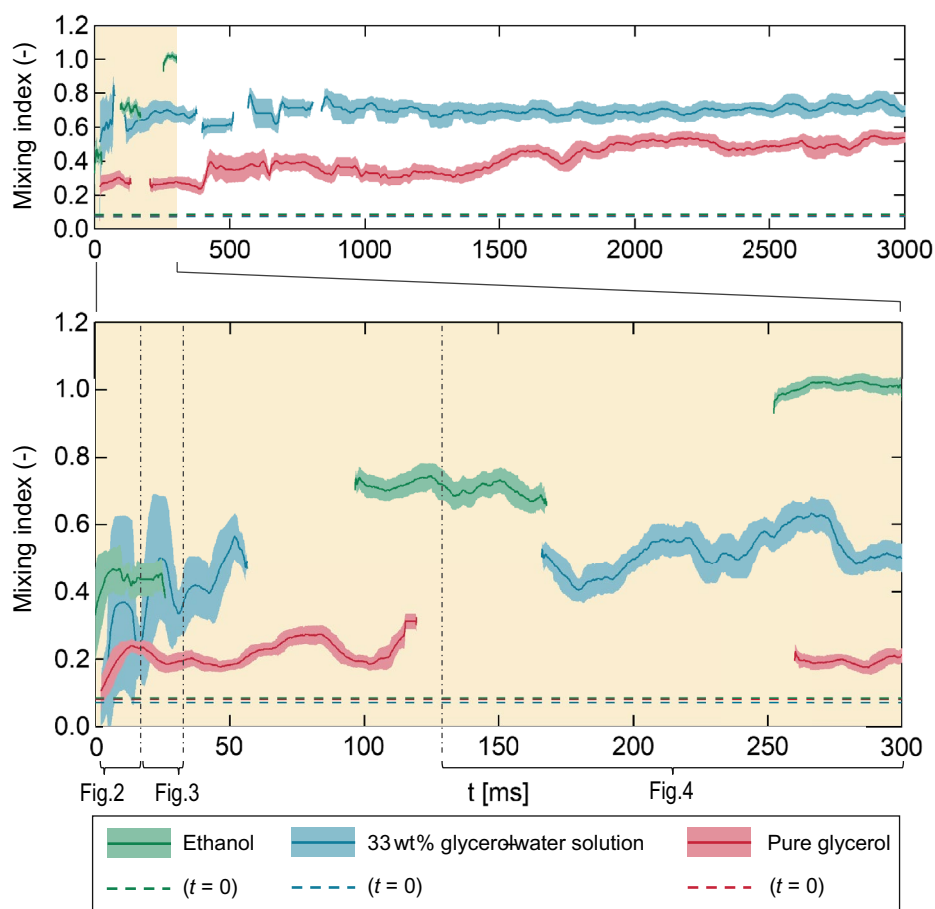
Figure 5. Time evolution of mixing index Mc after droplet coalescence. Lower figure shows the first 300 ms of the upper figure. Each solid line shows the moving average of 50 frames; the error band shows the standard deviation. Interruption in the lines correspond to when the droplet was outside the imaging area. Dashed lines correspond to the initial Mc's when the droplets coalesced at $t = 0$.

$t = 175$ ms. By contrast, $Mc = 0.5$ for the 33 wt% glycerol–water solution droplet, for which surface oscillation was no longer observed at $t = 125$ ms. Therefore, the aforementioned three factors are important for droplet mixing.

Summary
In this study, the fluid distribution and internal flow were measured simultaneously to understand the mixing dynamics of acoustically levitated airborne droplets. To accomplish this, we have developed a technique that selectively separates fluorescent particles within each fluid, and measures the concentration field based on the information derived from the discrete particle distribution. The proposed method presents a valuable tool for probing the relationship between the flow field and mixing, particularly for contactless quantitative study of physicochemical phenomena. Furthermore, it can significantly enhance our understanding of unsteady-state fluid dynamics in scenarios with time-induced volume and concentration variations.

Although we identified the relationship between surface oscillation and degree of mixing of acoustically levitated droplets. The present results provide insights into the dynamics of acoustically levitated airborne droplets and will be useful in the study of microfluidic interfacial dynamics, flow fields, heat/mass transfer, and chemical reactions. Such investigations will allow the contactless selection and manipulation and optimal sample handling for future lab-on-a-drop applications.

Methods
Experimental setup
Acoustic levitation was implemented in this study using an ultrasonic phased array[17]. The focal points of sound can be generated at arbitrary positions by transmitting sound waves with a controlled phase; localised acoustic standing waves can then be generated near the focal points using a glass plate. We employed a 7×7 square transducer array consisting of 49 small ultrasonic transducers (Nippon Ceramic Co., Ltd, T4010B4). The diameter and frequency of the transducers were 10 mm and 40 kHz, respectively. To generate ultrasonic focal points, the phase of the sound transmitted from each transducer was controlled using a field-programmable gate array (FPGA) (Altera Co., Cyclone-IV DE0-Nano). Figure 6 shows the experimental setup. The focal length and distance
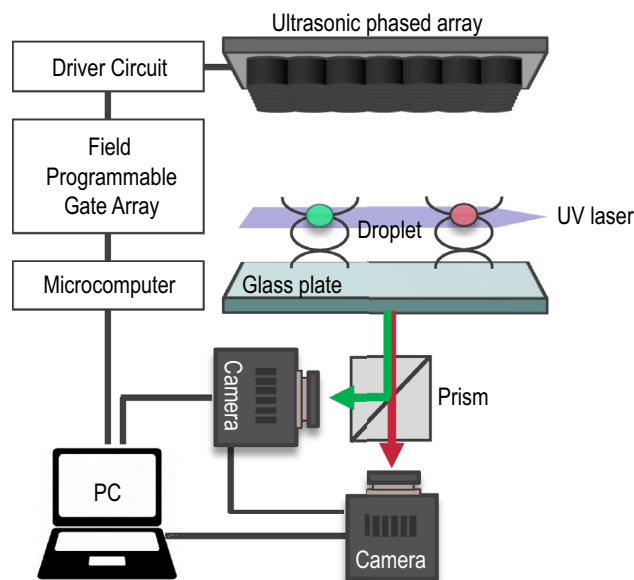
Figure 6. Schematic of experimental setup.
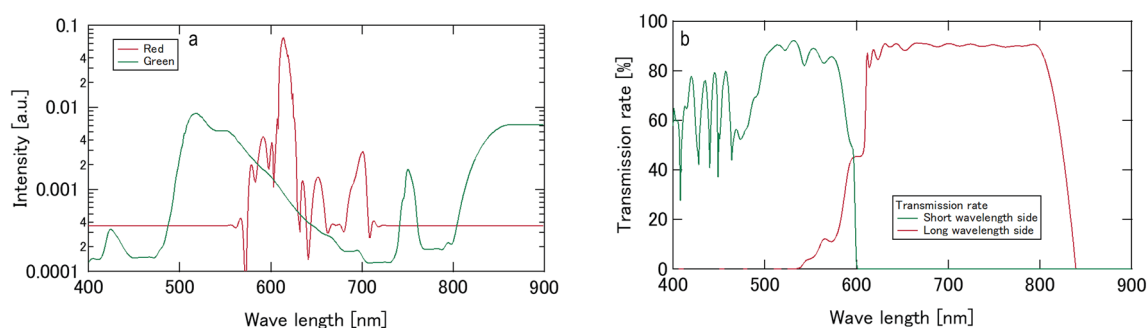
Figure 7. Characteristics of fluorescence and transmittance. (**a**) Fluorescent of tracer particle. (**b**) Transmittance of optical system.

from the transducer to the reflector were both 40 mm. Two droplets could be levitated by switching the focal points at a frequency of 500 Hz[17]. The levitated droplets can be transferred and coalesced by actively controlling the distance between the focal points[22]. The ambient temperature and relative humidity were 25.0 ± 0.5 ℃ and $40 \pm 10\%$, respectively. We used ethanol, 33 wt% glycerol–water solution, and pure glycerol to compare the effects of kinematic viscosity on the flow characteristics of a droplet with surface oscillation.

To visualise the flow and concentration fields inside the droplets, we employed red and green fluorescent acrylic particles from Central Techno Co. Ltd., known as Lumisis markers. These particles have an average diameter of 10 μm and a specific weight of 1.19. In comparison, the specific weights for ethanol, a 33 wt% glycerol–water solution, and pure glycerol are 1.51, 1.11, and 0.94 respectively. The density of the particles was suitably compatible with the fluid densities used in our study. The concentrations of both red and green particles were meticulously controlled to ensure they were identical. A UV sheet laser from Central Techno Co. Ltd. with a wavelength of 375 nm and a maximum power of 350 mW, was used to irradiate the cross-sections of droplets containing these fluorescent particles. The fluorescence characteristics are shown in Fig. 7(a). The behaviour of the two levitated droplets was monitored from below using a pair of synchronised monochromatic high-speed video cameras from Photron Co., Ltd. (FASTCAM-Mini AX200). These cameras were positioned on the short and long wavelength sides. Additionally, each camera was equipped with a short-pass filter (from THORLABS Co. Ltd., FESH0600) and a long-pass filter (from Kenko Co. Ltd., YA3). Figure 7(b) shows the transmittance of the optical system. To differentiate between the red and green fluorescent light emitted from the particles, a dichroic prism and optical long and short pass filters were employed. The frame rate was set at 6400 fps, with an exposure time of 1/6400 s.

In an effort to ascertain whether the mixing time of a solution can be observed through the use of particles in our study—particles that are several orders of magnitude larger than the size of molecules—we explored the mixing dynamics by considering physical timescales.
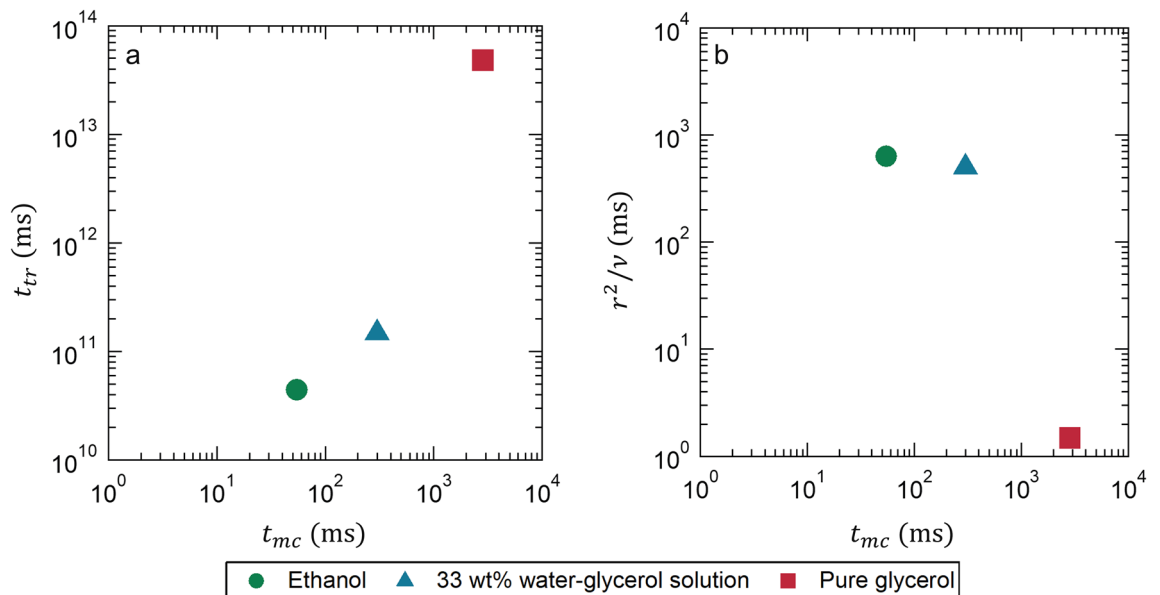
Figure 8. Comparison of physical timescales considered for droplet mixing. The mixing time $\underline{t_{mc}}$ for $Mc = 0.5$ (as shown in Fig. 5b) is compared with (**a**) the particle diffusion time t_{tr} and (**b**) the viscous dissipation time, both as functions of the droplet radius r and the kinematic viscosity v.

Figure 8 presents a comparison of these physical timescales considered for the process of droplet mixing. Initially, we introduced the diffusion timescale of the tracer particle, which is computed as follows:

$$t_{tr} = \frac{1}{D_{tr}}\left(\frac{d}{2}\right)^2,$$
$$\text{where } D_{tr} = \frac{k_B T}{6\pi \eta r_p} \tag{2}$$

where d is the equivalent diameter of droplets, k_B the Boltzmann constant, T, the absolute temperature, η, the viscosity of liquid, and r_p, the radius of the tracer particle. Figure 8a compares t_{mc} and t_{tr}; for all cases, $t_{tr} \gg t_{mc}$. This indicates that the mixing of tracer particles in the droplet was amplified by the internal flow resulting from droplet coalescence.

The internal flow was driven by the momentum transfer within the droplet, leading us to choose the viscous dissipation timescale as the second timescale for consideration. Figure 8b illustrates the relationship between t_{mc} and r^2/v. It is evident that t_{mc} decreases with a reduction in kinematic viscosity (or an increase of r^2/v). This suggests that momentum transfer was enhanced for droplets with lower viscosity, leading to a reduction in t_{mc} due to the impact of internal flow. Based on these findings, it can be concluded that advection is superior to molecular diffusion in terms of the mixing timescale in all cases we examined. As advection plays a pivotal role in solution mixing in our study, our methodology—predicated on particle colour—facilitates the measurement of concentration within localized areas of a droplet.

Image processing

For the visualisation of the mixing processes, images were developed by the following steps: (1) preparation of a set of pictures with dotted patterns; (2) calculation of the distortion and skew of images; (3) creation of correction functions for the distortion of each camera; (4) correction of image distortion for every picture obtained in the experiments; and (5) composition of the pictures into a single image.

For flow visualisation in the droplets, PIV was conducted using Koncerto II (Seika Digital Image Co., Japan).

Calculation of mixing index

To quantify the component distribution, an objective mixing index must be defined based on the number-density distribution of the particles. A schematic of the calculation procedure is shown in Fig. 9. First, the particles were detected from images taken by the high-speed video cameras (Fig. 9a). Next, the number fractions of neighbouring particles were used to calculate the number-fraction distribution, and a Voronoi diagram was developed accordingly, as shown in Fig. 9b. The particles were assumed to be adjacent when their respective Voronoi cells were in contact with each other (Fig. 9c). The number-fraction distribution in each cell was calculated as follows:

$$\theta_{p,j} = \frac{N_{p,j}}{\sum_p N_{p,j}}, \tag{3}$$
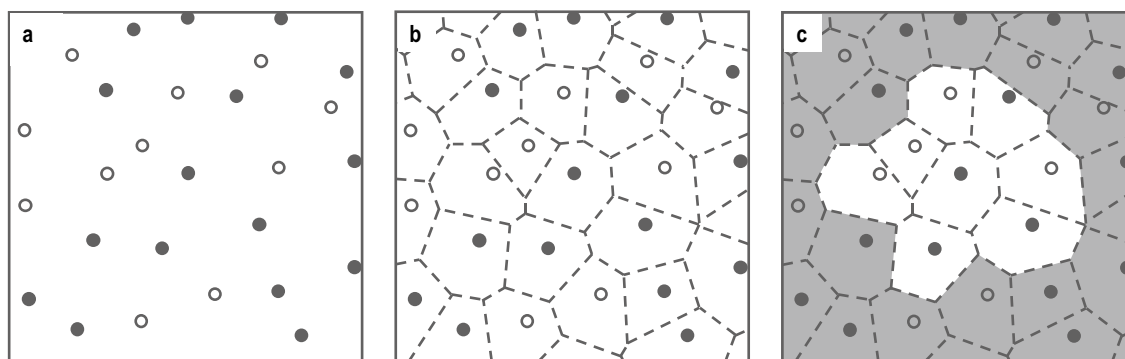
Figure 9. Procedure for calculating mixing index. (**a**) Detection of particles in image. (**b**) Corresponding Voronoi diagram. (**c**) Particles adjacent to central black particle. White or black circles represent red or green particles.

where θ is the number fraction, N, the number of neighbouring particles, p, the species of the particle, and j, the index of each particle.

To quantify the mixing state, we calculated Mc[52,53]:

$$M_C = \sum_p \frac{N_p}{\sum_p N_p} M_{c,p}, M_{c,p} = \frac{s_p^2 - s_{p,0}^2}{s_{p,R}^2 - s_{p,0}^2}, \tag{4}$$

where

$$
\begin{aligned}
s_p^2 &= \langle (\theta_{p,j} - \langle \theta_{p,j} \rangle)^2 \rangle, \\
s_{p,0}^2 &= \langle \theta_{p,j} \rangle (1 - \langle \theta_{p,j} \rangle), \\
s_{p,R}^2 &= \frac{\langle \theta_{p,j} \rangle (1 - \langle \theta_{p,j} \rangle)}{\langle n_j \rangle}.
\end{aligned}
\tag{5}
$$

Here, the number-fraction distribution $\theta_{p,j}$ is the local concentration of species p around particle j; n_j is the number of neighbouring particles around particle j; and s_p^2, $s_{p,0}^2$, and $s_{p,R}^2$ are the variances of the local particle-number fractions: s_p^2 is the variance at a given time, $s_{p,0}^2$, the variance at the initial time when the fluids were completely separated, and $s_{p,R}^2$, the variance at a time when the fluids were sufficiently mixed.

Data availability
The datasets generated and/or analysed during the current study are available from the corresponding author on reasonable request.

References
1. Ozcelik, A. *et al.* Acoustic tweezers for the life sciences. *Nat. Methods* **15**, 1021–1028 (2018).
2. Tsujino, S. & Tomizaki, T. Applications of acoustic levitation in chemical analysis and biochemistry. In *Acoustic Levitation: From Physics to Applications* (ed. Zang, D.) 151–179 (Springer, 2020).
3. Santesson, S. & Nilsson, S. Airborne chemistry: Acoustic levitation in chemical analysis. *Anal. Bioanal. Chem.* **378**, 1704–1709 (2004).
4. Priego-Capote, F. & de Castro, L. Ultrasound-assisted levitation: Lab-on-a-drop. *Trends Anal. Chem.* **25**, 856–867 (2006).
5. Crawford, E. A., Esen, C. & Volmer, D. A. Real time monitoring of containerless microreactions in acoustically levitated droplets via ambient ionization mass spectrometry. *Anal. Chem.* **88**, 8396–8403 (2016).
6. Puskar, L. *et al.* Raman acoustic levitation spectroscopy of red blood cells and *Plasmodium falciparum* trophozoites. *Lab Chip* **7**, 1125–1131 (2007).
7. Wood, B. R. *et al.* A portable Raman acoustic levitation spectroscopic system for the identification and environmental monitoring of algal cells. *Anal. Chem.* **77**, 4955–4961 (2005).
8. van Wasen, S., You, Y., Beck, S., Riedel, J. & Volmer, D. A. Quantitative analysis of pharmaceutical drugs using a combination of acoustic levitation and high resolution mass spectrometry. *Anal. Chem.* **93**, 6019–6024 (2021).
9. Benmore, C. J. & Weber, J. K. R. Amorphization of molecular liquids of pharmaceutical drugs by acoustic levitation. *Phys. Rev. X* **1**, 011004 (2011).
10. Barbosa, E. J. *et al.* Acoustic levitation and high-resolution synchrotron X-ray powder diffraction: A fast screening approach of niclosamide amorphous solid dispersions. *Int. J. Pharm.* **602**, 120611 (2021).
11. Morris, R. H. *et al.* Non-contact universal sample presentation for room temperature macromolecular crystallography using acoustic levitation. *Sci. Rep.* **9**, 12431 (2019).
12. Vasileiou, T., Foresti, D., Bayram, A., Poulikakos, D. & Ferrari, A. Toward contactless biology: Acoustophoretic DNA transfection. *Sci. Rep.* **6**, 20023 (2016).
13. Andrade, M. A. B., Okina, F. T. A., Bernassau, A. L. & Adamowski, J. C. Acoustic levitation of an object larger than the acoustic wavelength. *J. Acoust. Soc. Am.* **141**, 4148–4154 (2017).

14. Andrade, M. A. B., Marzo, A. & Adamowski, J. C. Acoustic levitation in mid-air: Recent advances, challenges, and future perspectives. *Appl. Phys. Lett.* **116**, 250501 (2020).
15. Xie, W. J., Cao, C. D., Lü, Y. J., Hong, Z. Y. & Wei, B. Acoustic method for levitation of small living animals. *Appl. Phys. Lett.* **89**, 214102 (2006).
16. Foresti, D., Sambatakakis, G., Bottan, S. & Poulikakos, D. Morphing surfaces enable acoustophoretic contactless transport of ultrahigh-density matter in air. *Sci. Rep.* **3**, 3176 (2013).
17. Marzo, A. *et al.* Holographic acoustic elements for manipulation of levitated objects. *Nat. Commun.* **6**, 8661 (2015).
18. Zang, D. *et al.* Inducing drop to bubble transformation via resonance in ultrasound. *Nat. Commun.* **9**, 3546 (2018).
19. Zhang, S. P. *et al.* Digital acoustofluidics enables contactless and programmable liquid handling. *Nat. Commun.* **9**, 2928 (2018).
20. Drinkwater, B. W. A Perspective on acoustical tweezers—devices, forces, and biomedical applications. *Appl. Phys. Lett.* **117**, 180501 (2020).
21. Yang, Z. *et al.* Light sheet microscopy with acoustic sample confinement. *Nat. Commun.* **10**, 669 (2019).
22. Watanabe, A., Hasegawa, K. & Abe, Y. Contactless fluid manipulation in air: Droplet coalescence and active mixing by acoustic levitation. *Sci. Rep.* **8**, 1–8 (2018).
23. Andrade, M. A. B., Camargo, T. S. A. & Marzo, A. Automatic contactless injection, transportation, merging, and ejection of droplets with a multifocal point acoustic levitator. *Rev. Sci. Instrum.* **89**, 125105 (2019).
24. Tsujino, S., Shinoda, A. & Tomizaki, T. On-demand droplet loading of ultrasonic acoustic levitator and its application for protein crystallography experiments. *Appl. Phys. Lett.* **114**, 213702 (2019).
25. Hasegawa, K., Watanabe, A., Kaneko, A. & Abe, Y. Coalescence dynamics of acoustically levitated droplets. *Micromachines* **11**, 343 (2020).
26. Chen, G. *et al.* Towards the rapid and efficient mixing on 'open-surface' droplet-based microfluidics via magnetic actuation. *Sens. Actuators B Chem.* **286**, 181–190 (2019).
27. Ward, K. & Fan, Z. H. Mixing in microfluidic devices and enhancement methods. *J. Micromech. Microeng.* **25**, 094001 (2015).
28. Ottino, J. M. & Wiggins, S. Introduction: Mixing in microfluidics. *Philos. Trans. R. Soc. A Math. Phys. Eng. Sci.* **362**, 923–935 (2004).
29. Sasaki, Y., Hasegawa, K., Kaneko, A. & Abe, Y. Heat and mass transfer characteristics of binary droplets in acoustic levitation. *Phys. Fluids* **32**, 072102 (2019).
30. Zang, D. *Acoustic Levitation* (ed. Zang, D.), (Springer Nature, Singapore, 2020)
31. Koyano, Y. *et al.* Diffusion enhancement in a levitated droplet via oscillatory deformation. *Phys. Rev. E* **102**, 1–10 (2020).
32. Fang, Z., Huang, X., Taslim, M. E. & Wan, K. Flexural bending resonance of acoustically levitated glycerol droplet. *Phys. Fluids* **33**, 071701 (2021).
33. Hasegawa, K., Watanabe, A., Kaneko, A. & Abe, Y. Internal flow during mixing induced in acoustically levitated droplets by mode oscillations. *Phys. Fluids* **31**, 112101 (2019).
34. Shen, C. L., Xie, W. J. & Wei, B. Parametrically excited sectorial oscillation of liquid drops floating in ultrasound. *Phys. Rev. E* **81**, 1–6 (2010).
35. Shen, C. L., Xie, W. J., Yan, Z. L. & Wei, B. Internal flow of acoustically levitated drops undergoing sectorial oscillations. *Phys. Lett. A Gen. At. Solid State Phys.* **374**, 4045–4048 (2010).
36. Tian, Y. S. *et al.* Coalescence time of water-in-oil emulsions under shear. *Chem. Eng. Sci.* **250**, 117257 (2022).
37. Chireux, V., Tordjeman, P. & Risso, F. Bridge expansion after coalescence of two droplets in air: Inertial regime. *Phys. Fluids* **33**, 062112 (2021).
38. Paulsen, J. D., Carmigniani, R., Kannan, A., Burton, J. C. & Nagel, S. R. Coalescence of bubbles and drops in an outer fluid. *Nat. Commun.* **5**, 3182 (2014).
39. Kim, J. & Longmire, E. K. Investigation of binary drop rebound and coalescence in liquids using dual-field PIV technique. *Exp. Fluids* **47**, 263–278 (2009).
40. Gotaas, C. *et al.* Effect of viscosity on droplet-droplet collision outcome: Experimental study and numerical comparison. *Phys. Fluids* **19**, 102106 (2007).
41. Shuravin, N. S., Dolganov, P. V. & Dolganov, V. K. Coalescence of viscous two-dimensional smectic islands. *Phys. Rev. E* **99**, 062702 (2019).
42. Qian, J. & Law, C. K. Regimes of coalescence and separation in droplet collision. *J. Fluid Mech.* **331**, 59–80 (1997).
43. Jin, J., Ooi, C. H., Dao, D. V. & Nguyen, N.-T. Coalescence processes of droplets and liquid marbles. *Micromachines* **8**, 336 (2017).
44. Eggers, J., Lister, J. R. & Stone, H. A. Coalescence of liquid drops. *J. Fluid Mech.* **401**, 293–310 (1999).
45. Klopp, C. & Eremin, A. On droplet coalescence in quasi-two-dimensional fluids. *Langmuir* **36**, 10615–10621 (2020).
46. Aarts, D. G. A. L., Lekkerkerker, H. N. W., Guo, H., Wegdam, G. H. & Bonn, D. Hydrodynamics of droplet coalescence. *Phys. Rev. Lett.* **95**, 164503 (2005).
47. Ottino, J. M. *The Kinematics of Mixing: Stretching, Chaos, and Transport* (Cambridge University Press, 1989).
48. Suh, Y. K. & Kang, S. A review on mixing in microfluidics. *Micromachines* **1**, 82–111 (2010).
49. Bowler, A. L., Bakalis, S. & Watson, N. J. A review of in-line and on-line measurement techniques to monitor industrial mixing processes. *Chem. Eng. Res. Des.* **153**, 463–495 (2020).
50. Nilsson, M. A. & Rothstein, J. P. The effect of contact angle hysteresis on droplet coalescence and mixing. *J. Colloid Interface Sci.* **363**, 646–654 (2011).
51. Lamb, H. *Hydrodynamics* 6th edn, 473–475 (Cambridge University Press, 1932).
52. Lacey, P. M. C. Developments in the theory of particle mixing. *J. Appl. Chem.* **4**, 257–268 (2007).
53. Zhang, Z., Gui, N., Ge, L. & Li, Z. Numerical study of particle mixing in a tilted three-dimensional tumbler and a new particle-size mixing index. *Adv. Powder Technol.* **30**, 2338–2351 (2019).

Acknowledgements

Author contributions

A.K. and Y.A. designed the research; K.Ho. performed the research; K.Ho. and K.F. built the setup and analysed the data; and K.Ho., K.F. and K.Ha. wrote the manuscript. All authors supplied comments and approved the final version of the manuscript.

Competing interests

The authors declare no competing interests.

Additional information

Supplementary Information The online version contains supplementary material available at https://doi.org/10.1038/s41598-023-46008-z.

Correspondence and requests for materials should be addressed to A.K.

Reprints and permissions information is available at www.nature.com/reprints.

Publisher's note Springer Nature remains neutral with regard to jurisdictional claims in published maps and institutional affiliations.